# A Fluid–Structure Interaction Study on a Bionic Fish Fin With Non-Uniform Stiffness Distribution

**Yang Luo**
Department of Naval Architecture, Ocean and Marine Engineering, University of Strathclyde, Glasgow G4 0LZ, UK
e-mail: y.luo@strath.ac.uk

**Qing Xiao**[1]
Department of Naval Architecture, Ocean and Marine Engineering, University of Strathclyde, Glasgow G4 0LZ, UK
e-mail: qing.xiao@strath.ac.uk

**Guangyu Shi**
Department of Naval Architecture, Ocean and Marine Engineering, University of Strathclyde, Glasgow G4 0LZ, UK
e-mail: guangyu.shi@strath.ac.uk

*In this paper, the propulsive performance of a caudal peduncle-fin swimmer mimicking a bio-inspired robotic fish model is numerically studied using a fully coupled FSI solver. The model consists of a rigid peduncle and a flexible fin which pitches in a uniform flow. The flexible fin is modeled as a thin plate assigned with non-uniformly distributed stiffness. A finite volume method based in-house Navier–Stokes solver is used to solve the fluid equations, while the fin deformation is resolved using a finite element code. The effect of the fin flexibility on the propulsive performance is investigated. The numerical results indicate that compliance has a significant influence on performance. Under the parameters studied in this paper, the medium flexible fin exhibits remarkable efficiency improvement, as well as thrust augment, while the least flexible fin shows no obvious difference from the rigid one. However, for the most flexible fin, although the thrust production decreases sharply, the efficiency reaches the maximum value. It should be noted that by non-uniformly distributing the rigidity across the caudal fin, our model is able to replicate some fin deformation patterns observed in both the live fish and the experimental robotic fish.*
[DOI: 10.1115/1.4046409]

*Keywords: computational fluid dynamics, fluid–structure interaction, hydrodynamics*

## 1 Introduction

The ocean is rich in abundant resources such as minerals, natural gas, and many others that benefit humans. The bio-inspired underwater vehicle, as a new type of artificial vehicle, is a promising tool to explore and exploit the ocean. The advantages of such vehicles include low noise generation, excellent maneuverability, and high efficiency at low-speed cruising [1,2]. The fin-activated propulsion of aquatic animals provides a good prototype for the design of biomimetic propellers due to the simple mechanical implementation. Among them, the caudal fin propulsion is widely imitated in the design of underwater vehicle [3].

In the past studies, to understand the fundamental locomotion mechanism of the fish propulsion, the flexible fish fin or body were usually simplified as rigid models [4,5]. More recently, the flexible impact on the propulsive performance was investigated and the results showed improved performance compared with a rigid model. However, the so-called "flexibility" in those studies refers to a mathematically pre-defined fin deformation by reconstructing the realistic kinematics observed/recorded from the live fish experiment [6–8]. In such a way, only the hydrodynamic response to the designated structure deformation was examined, whereas the effect of resultant fluid forces on the flexible fins was neglected. Through the consideration of the dynamic interplay between the flexible fins and the immersed fluid medium, some studies explored the effect of the stiffness on the propulsive performance of the fins. These studies usually considered flexible fins with uniformly distributed structural parameters [9,10]. However, a real fish fin is characterized as a composite structure composed of a membrane strengthened by fin rays [11]. Therefore, the simplified fin models with uniformly distributed stiffness may be unable to reflect the real fin's propulsive performance and its bending pattern.

To further understand the fundamental mechanism of fish swimming associated with physical properties, some experiments and numerical simulations have been conducted to investigate the correlation between the inhomogeneous distribution of a caudal fin's rigidity and its propulsion capabilities. For example, a novel variable-stiffness flapping mechanism was implemented in the design of a bio-inspired underwater robot by Park et al. [12]. Their experimental results reported the improvement of the efficiency attributed to this unique design. The stiffness profiles of real fish were measured by Kancharala and Philen using digital image correlation techniques [13]. With their experimental data, a chordwise varying stiffness robotic fin was fabricated to study the locomotion performance in a water tunnel. Their results indicated that the fins with varying stiffness generated larger thrusts and higher efficiency compared with the uniform ones.

Numerically, due to the complexity to resolve three-dimensional and time-dependent structural deformation and the resultant surrounded fluid flow, few numerical simulations were conducted to investigate the dynamic interaction of the flexible fins and fluid. For example, Zhu and Bi developed a fully coupled FSI model to study the spanwise deformation on the dynamics of a ray-supported swaying caudal fin, and the performance enhancement through the specific non-uniform distribution of rigidity on the fin was reported [14].

However, the effect of the peduncle is often ignored in the previous studies on caudal fin propulsion, while it does exist in real fish locomotion [15]. In addition, the research on the influence of stiffness reinforcement due to the fin rays is very limited in the existing FSI simulations, while the experimental results by Esposito et al. [16] suggested that on account of the existence of rays and thus the different stiffness of fin surface, the deformation of fin is not truly flat. In this work, inspired by the experiment conducted by Ren et al. [17], a model composed of a rigid peduncle and a flexible caudal fin with non-uniform flexibility is built to investigate the impact of three-dimensional deformation on fin's propulsive performance through a fully coupled FSI numerical solver. Here, the homocercal fin is modeled as an elastic thin plate assigned with inhomogeneous rigidity, in which the rays-surrounding area is

[1]Corresponding author.

Contributed by the Ocean, Offshore, and Arctic Engineering Division of ASME for publication in the Journal of Offshore Mechanics and Arctic Engineering. Manuscript received August 6, 2019; final manuscript received December 18, 2019; published online February 19, 2020. Assoc. Editor: Yanlin Shao.

strengthened. The main objective of this study is to validate our newly developed FSI solver and then investigate how the compliance affects the propulsion performance of a caudal fin behind a locomotor peduncle.

## 2 Mathematical Model and Numerical Approach

In this section, the governing equations for the fluid and the solid are described. The fluid and structural domains are represented by $\Omega_f$ with the boundary $\Gamma_f$ and $\Omega_s$ with $\Gamma_s$, respectively. The fluid–structure interface $\Gamma_i = \Gamma_f \cap \Gamma_s$ between the fluids and structures is the common boundary of the two domains.

**2.1 Fluid Solver.** The governing equations of the flow around the caudal peduncle and fin can be expressed in the integral form as

$$\frac{\partial}{\partial t}\iiint_{\Omega_f} \mathbf{W} d\Omega_f + \oiint_{\Gamma_f} (\mathbf{F}_c - \mathbf{F}_d)\cdot \mathbf{n} d\Gamma_f = 0 \tag{1}$$

where $\mathbf{n}$ is the unit normal vector in the outward direction, $\mathbf{W}$ represents the conservative variable vector, the vector $\mathbf{F}_c$ is the convective flux, and the diffusion flux is denoted by $\mathbf{F}_d$.

The in-house fluid solver solves the viscous, compressible flow using a cell-centered finite volume method based on a multi-block grid system. Using a structured methodology, the fluid domain $\Omega_f$ is divided into an array of hexahedral cells. The convective term is discretized by a central Jameson–Schmidt–Turkel scheme with an artificial dissipative term introduced by Jameson et al. [18]. Green's theorem is applied to obtain the first-order derivatives calculating the viscous flux tensors. For unsteady simulations, the dual-time stepping algorithm is used for time integration [19].

Furthermore, the local time stepping and multigrid method are implemented in the fluid solver to accelerate the convergence and implicit residual smoothing is applied to increase the stability of the solution. Parallelization is achieved via message passing interface to enable large-scale computation.

It is noted that in this study, the freestream Mach number, defined as $\mathrm{Ma}_\infty = U/a_\infty$, where $U$ is the flow velocity and $a_\infty$ is the speed of sound of the free stream respectively, is chosen as 0.06 to ensure that the compressibility of the fluid is negligibly small but still large enough for numerical stability. Additionally, the local Mach numbers of the whole computational domain are monitored to guarantee that they are always below the critical value for pronounced compressibility ($\mathrm{Ma} = 0.3$). This compressible fluid solver has been successfully applied to study various incompressible fluid problems in our previous work [20–23].

**2.2 Structural Solver.** The basic equation of the finite element method in the weak form of the balance of momentum can be written in the differential form as

$$\rho_s \frac{D^2\mathbf{U}}{D^2t^2} = \nabla\cdot\mathbf{P} + \rho_s\mathbf{f} \tag{2}$$

where the acceleration of the material point is obtained by the second derivatives of the displacement vector $\mathbf{U}$ of the structure. Surface forces are modeled by the second Piola-Kirchoff stress tensor $\mathbf{P}$ and body forces of per unit mass such as gravity are represented by $\mathbf{f}$. The solid density is denoted by $\rho_s$.

The general governing equations of the solid dynamics, i.e., Eq. (2), are discretized using the finite element method. By applying the standard virtual work method, the linear algebraic equation system can be obtained by discretizing Eq. (2) in the whole solid domain as

$$[\mathbf{K}]\{\mathbf{U}\} + [\mathbf{M}]\frac{D^2}{Dt^2}\{\mathbf{U}\} = \{\mathbf{F}\} \tag{3}$$

where $[\mathbf{K}]$ is the global stiffness matrix, $[\mathbf{M}]$ is the global matrix, and $[\mathbf{F}]$ is the global force vector. By applying Newton's second law of motion, the time domain is discretized using the $\alpha$-method with a second-order accuracy here.

In the present work, the implementation of finite element method solver is based on CalculiX written by Dhondt [24], in which a variety of element types including the brick element, the tetrahedral element, and the wedge element are used to discretize the solid domain and define the shape functions.

**2.3 Fluid–Structure Coupling.** Considering the fluid solver [25] and CalculiX [24] are both highly specialized in its specific single-field physical solution and provide some advanced features, a partitioned coupling scheme is thus employed in order to keep the advantages from both solvers. In the present partitioned framework, an implicit scheme is designed to avoid the numerical instability that may be encountered when the mass ratio is low. In the present work, the fluid solver is integrated with CalculiX via Precise Code Interaction Coupling Environment (preCICE), a coupling library for partitioned multi-physics simulations [26].

In this solver, the interface quasi-Newton method with inverse Jacobian from a least-squares model (IQN-ILS) [27,28] implemented in preCICE is used to stabilize the coupling and accelerate the convergence. It is a Newton–Raphson scheme which tries to find the root of the residual equations of displacements and fluid forces at the interface. Figure 1 demonstrates the basic coupling procedure where a sub-iteration loop is introduced within each time-step $n$. Within each sub-iteration, the fluid grid is updated via a fast-moving mesh algorithm [29]. The communication between the fluid and structural solver is established via Transmission Control Protocol/Internet Protocol (TCP/IP) sockets, and the data mapping is achieved by the radial basis functions-based interpolation [30]. The details of the framework of the present FSI solver are described in Ref. [31].

## 3 The Flexible Caudal Fin Problem Formulation

The current peduncle and caudal fin model is inspired by the experiment test conducted by Ren et al. [17], where a robotic fishtail mimicking the locomotion of the Bluegill Sunfish (*Lepomis macrochirus*) has been experimentally examined. In their experiment, the robot consists of a rigid peduncle and a flexible caudal fin, and more details of the experimental setup can be found in Ref. [17].

In this work, the geometry and dimensions of the peduncle and caudal fin is depicted in Fig. 2, where the geometrical data of the caudal fin is taken from the experiment [17] which is designed to replicate the shape of its real biological counterpart [32]. However, the peduncle is modified, as displayed in Fig. 2, to present a streamlined fashion and a smooth transition from the peduncle to caudal fin, which mimics a real fishtail and also provides the ease for our computational fluid dynamics (CFD) mesh generation.

The kinematics of the present model is described as follows. The peduncle combined with the caudal fin rotates harmonically around the $z$-axis with the reference point $\boldsymbol{O}$ in a uniform flow in the positive $x$-direction with a velocity of $U$. The time-dependent pitch motion of the model is described by $\theta(t) = \theta_m \sin(2\pi f t)$, where $\theta_m$ is the maximum amplitude and $f$ denotes the oscillating frequency.

The dimensionless parameters are defined as the Reynolds number $\mathrm{Re} = Uc/\nu$, where $c$ is the maximum chord length of the fin at the angle of 37.5 deg; mass ratio $m^* = \rho_s t/\rho_f c$; the reduced frequency $f^* = fc/U$; the Poisson's ratio the $\nu_s$; dimensionless stiffness $K = EI/(\rho_f U^2 c^3)$, where $E$ is Young's modulus and $I = h^3/12$ is the area moment of inertia of the cross section.

**3.1 Performance Metrics.** To evaluate the propulsion performance of the caudal fin, the instantaneous thrust and power coefficients are defined as

$$C_T = -\frac{F_x}{\frac{1}{2}\rho_f U^2 S} \tag{4}$$

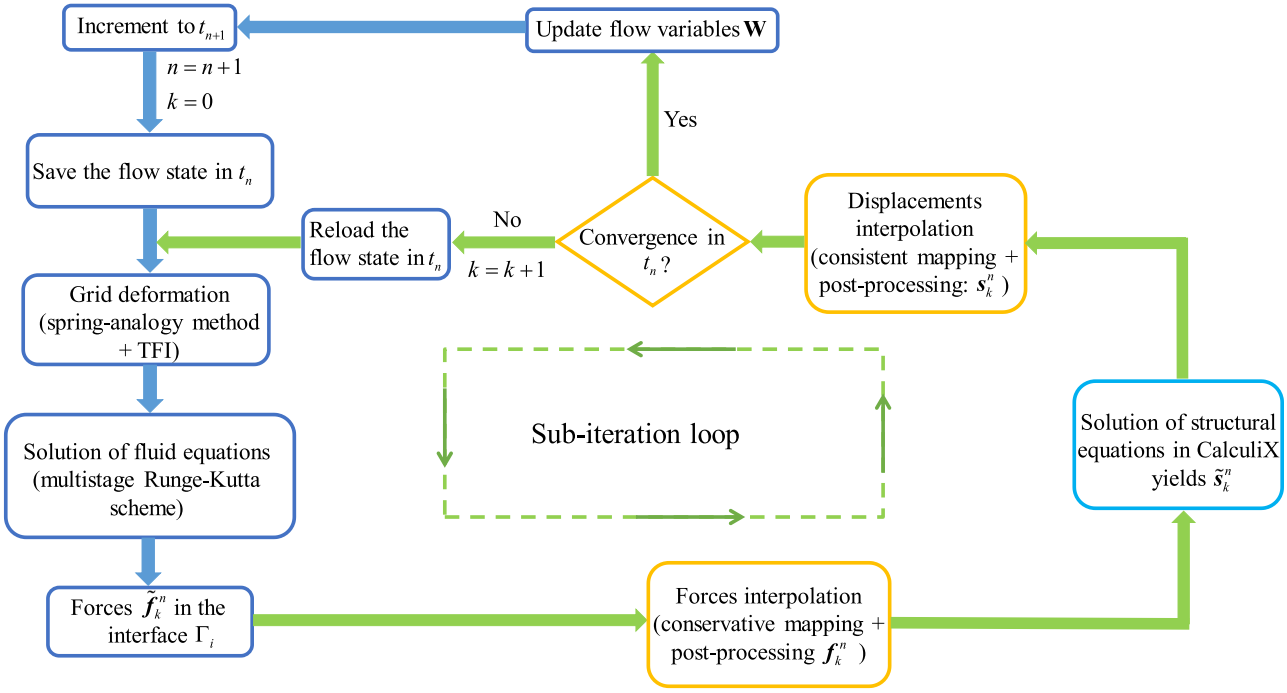


**Fig. 1 Flowchart of the implicit FSI coupling in a partitioned approach adapted from Ref. [31]**

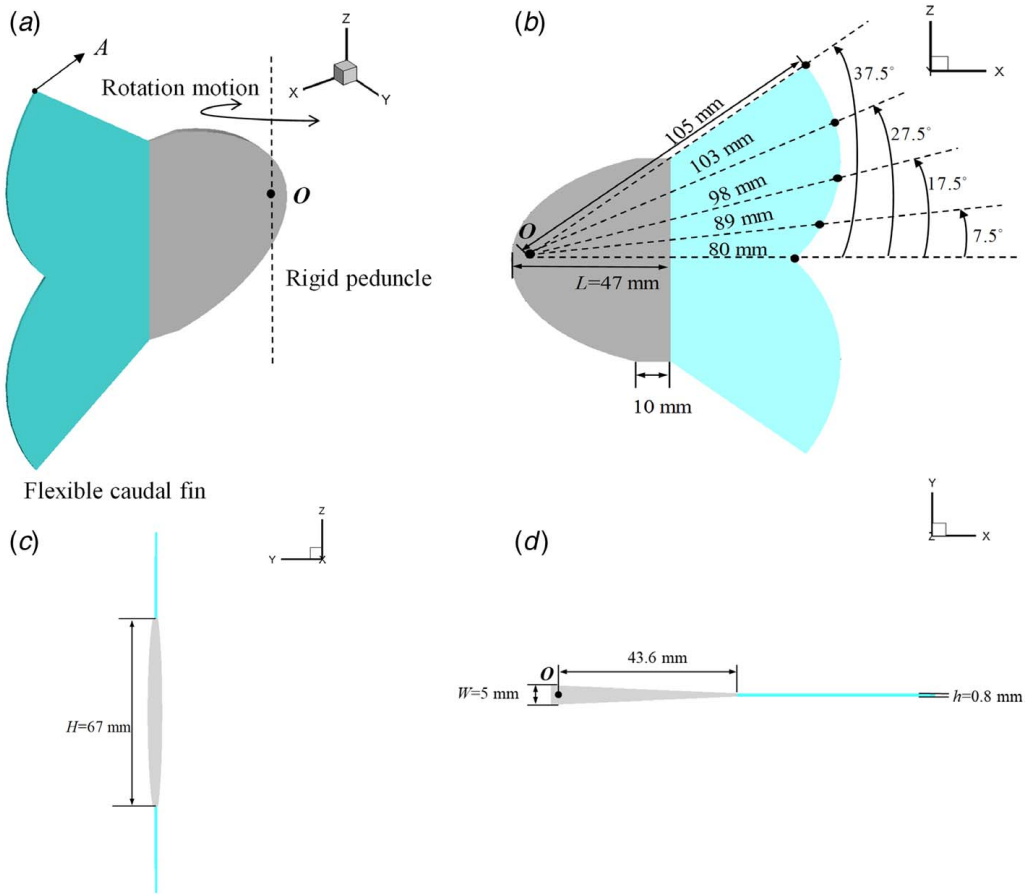


**Fig. 2 The peduncle and caudal fin model and dimensions: (*a*) fish peduncle-caudal model, (*b*) *xz* view of the model and dimensions, (*c*) *yz* view of the model and dimensions, and (*d*) *xy* view of the model and dimensions**

$$C_P = \frac{M_O \dot{\theta}}{\frac{1}{2}\rho_f U^3 S} \tag{5}$$

where $F_x$ is the total hydrodynamic forces on the caudal fin in the $x$-direction, $S$ is the reference area, i.e., the area of the fin in the $xz$ surface, and $M_O$ represents the $z$-component of the reaction moment at point $O$. Meanwhile, the lateral force is defined as the hydrodynamic force in the $y$-direction

$$C_L = \frac{F_y}{\frac{1}{2}\rho_f U^2 S} \tag{6}$$

The propulsion efficiency $\eta$ is given by

$$\eta = \frac{\bar{C}_T}{\bar{C}_P} \tag{7}$$

where $\bar{C}_T$ and $\bar{C}_P$ are the time-averaged values of $C_T$ and $C_P$ within one oscillating period.

**3.2 Structural Model of the Caudal Fin—The Non-Uniformity of Flexible Fins.** In the experiment by Ren et al. [33], the fin consists of rigid rays and elastic membrane. The fin membrane is glued with the rays. Since the rays are relatively much smaller compared with the whole fin membrane surface, therefore, to simplify the modeling, the rays are not modeled explicitly in the present simulation. Nevertheless, considering the existence of the rigid rays, the stiffness of the caudal fin is strengthened locally surrounding the glued rays.

To consider the effect of the rays on the fin membrane, non-uniform distribution of Young's modulus is assigned to the finite element model of the fin, as depicted in Fig. 3. The non-dimensional stiffness around the fin rays area $K_1$ is larger than that $K_2$ away from these areas, and $K_1 = rK_2$, $r > 1$, where $r$ is the stiffness ratio. By referencing the distribution of the material properties of a caudal fin inversely determined by Liu et al. [34] using a finite element analysis method, the stiffness ratio is selected as $r = 2$.

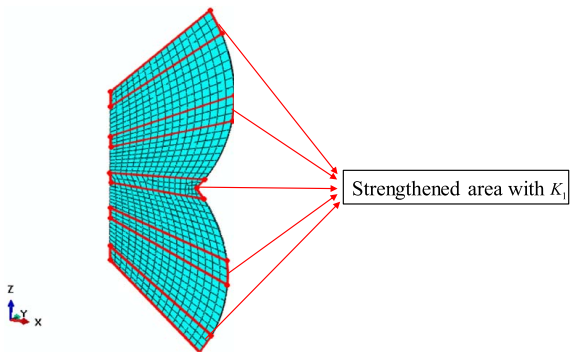


**Fig. 3 The generated structural finite element mesh with the locally strengthened area of the caudal fin**

## 4 Validation and Resolution Verification

**4.1 Validation Cases.** The fluid solver used in the present work has been extensively validated in our previous work [20–22,25]. Here, the following three properly selected cases are used to validate the coupling of the fluid solver with CalculiX via preCICE.

*4.1.1 Flow Over a Flexible Cantilever Behind a Square Cylinder.* This problem consists of a fixed square bluff body with an elastic cantilever attaching in its wake [35–37]. Previous studies indicated that the flow separated from the leading edge of the square cylinder will induce a periodic oscillation of the flexible cantilever.

The layout of the computational domain is presented in Fig. 4(*a*). In the present simulation, three grids are generated using a multi-block approach, i.e., a fine mesh with 153,428 cells, a medium mesh with 110,284 cells and a coarse one with 77,556 cells. The structural mesh comprises 123 quadratic wedge elements with standard shape functions [24].

In this simulation, $\mathrm{Re} = U_\infty d/\nu = 330$, therefore, the laminar flow is solved. The physical properties, i.e., mass ratio $m^* = \rho_s e/\rho_f l = 1.27$, non-dimensional bending stiffness $K = EI/(\rho_f U_\infty^2 l^3) = 0.23$, and Poisson's ratio $\nu_s = 0.35$ are chosen to make the frequency of shedding vortex approximate the first eigen-frequency of the cantilever so that a remarkable oscillation can be observed. In the structural part, the left end of the cantilever is set as fixed, and the movement of the whole cantilever is limited only in $x$- and $y$-directions.

Figure 5 depicts the displacement of the free end of the flexible beam in the $y$-direction with three dimensionless time-step sizes, which are defined as $\overline{\Delta t} = \Delta t U_\infty/d$, for the three different meshes. As seen, the displacement lies in a range of 0.80–1.20 cm, and the non-dimensional oscillation period $\bar{T} = TU_\infty/d$ varies around 16.01. Observed from previously published literature [35,36,38–40], the displacement amplitude lies between 0.8 and 1.4 cm and $\bar{T}$ ranges between 15.80 and 17.44. Therefore, the current simulation results have a good agreement with the previous numerical solution.

The generated mesh after deformation when the tip displacement reaches its maximum is depicted in Fig. 4(*b*). The velocity and pressure contours around the square cylinder and the cantilever at this moment are shown in Fig. 6. The velocity distribution presents the unsteady behavior of the flow, especially around the cylinder and cantilever. Small velocity magnitudes are observed

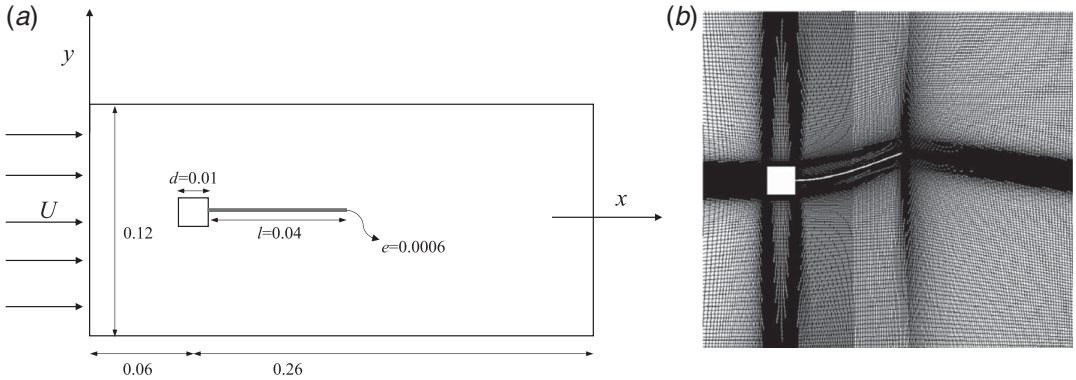


**Fig. 4 The computational domain layout (*a*) adopted from Ref. [31], and the generated medium mesh around the cantilever after the deformation when the tip displacement reaches the maximum (*b*)**

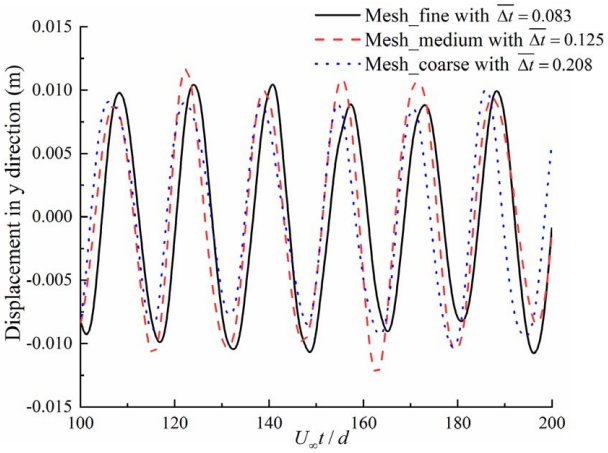


**Fig. 5 Vertical tip displacement of the cantilever beam with different time-step sizes**

near the cantilever and cylinder surfaces which is consistent with the results in Ref. [38]. It is also observed that the pressure difference between the upper and lower surface of the cantilever is pronounced, which may contribute to the unsteady oscillation of the cantilever directly.

*4.1.2 The Bending of a Three-Dimensional Flexible Plate in Uniform Flow.* In this validation test, it involves a flexible plate which is bent while placed in crossflow. The original case derives from an experimental study on the flow-induced reconfiguration of flexible aquatic vegetation conducted by Luhar and Nepf [41]. One of their experiment cases was then numerically simulated as an FSI validation by Tian et al. [42]. In their work, they quantitatively compared the results with experimental data in the presence of gravity and buoyancy and performed a series of simulations in the absence of them for the purpose of benchmarks studies. Here, the latter cases are chosen to validate our proposed multi-physics numerical suite.

The computational domain of the flow over the elastic plate is depicted in Fig. 7(*a*). The plate is placed vertically in the crossflow with its bottom end clamp-mounted while the free end can deform under the action of fluid forces. The parameters are all dimensionless: the length $h = 5b$, the thickness $t = 0.2b$, where $b$ is the width, the flow is laminar and $\mathrm{Re} = U_0 h/\nu = 100$, mass ratio $m^* = \rho_s b/\rho_f\ t = 0.14$, $K = EI/\rho_f U_0^2 b^3 = 2.39$, and $\nu_s = 0.4$. The fluid computational domains contain three meshes including a coarse grid with 2,793,362 cells, a medium one with 3,916,111 grid cells, and a fine mesh with 5,585,602 cells. Three dimensionless time-step sizes, which are defined as $\overline{\Delta t} = \Delta t U_0/b$, i.e., $\overline{\Delta t} = 0.0292$, $\overline{\Delta t} = 0.0208$, and $\overline{\Delta t} = 0.0148$ are used for the computation, respectively. The structural mesh contains 1400 quadratic brick elements.

The displacement of the plate center and the drag coefficient, which is defined as $C_d = F_x/(0.5\rho_f U_0^2 bh)$, in the absence of gravity and buoyancy when $\mathrm{Re} = 100$ are compared in Table 1. Based on the results shown in Table 1, we also simulated the deformation of the plate under $\mathrm{Re} = 400$ using the medium mesh with $\overline{\Delta t} = 0.0208$ and the results are shown in Table 2. It indicates that the present FSI simulation results match well with the counterparts in Ref. [42].

*4.1.3 The Response of a Flexible Plate in a Forced Harmonic Heave Motion.* This numerical validation case involves an experimental study conducted by Paraz et al. [43,44]. It consists of a

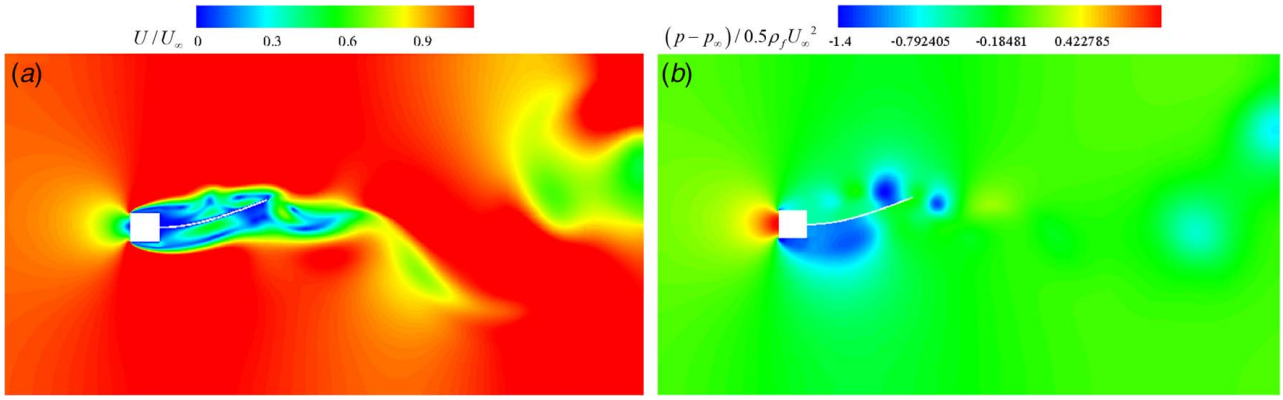


**Fig. 6 The velocity magnitude contour (*a*) and pressure contour around the cantilever when the tip displacement reaches the maximum (*b*)**

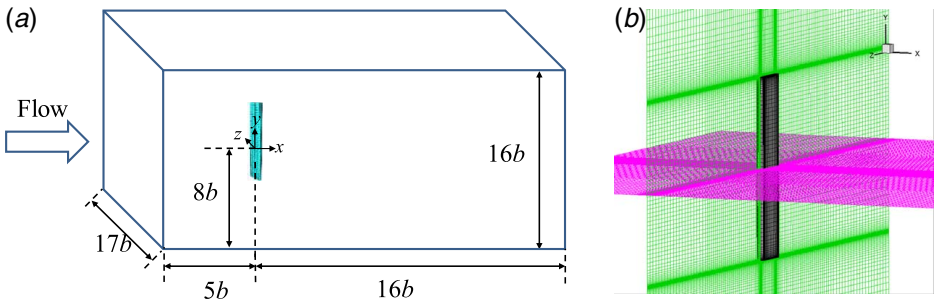


**Fig. 7 The computational domain of flow over an elastic plate (*a*) and the generated medium mesh around the plate (*b*)**

horizontal flexible plate which is made of the polysiloxane. The plate has a rounded leading edge and a tapered trailing edge. The thickness of the plate is 0.004 m, chord length is 0.12 m, and span is 0.12 m, giving an aspect ratio of 1. In their experiment, the leading edge was forced into a harmonic heave motion while the trailing edge was set free, as shown in Fig. 8(*a*). The elastic plate deformed under the hydrodynamic forces. More detail about the experimental setup can be found in Ref. [44].

Three grids are generated: a coarse mesh with 40,626 cells, a medium-size mesh with 57,424 cells, and a fine mesh with 79,514 cells. With these fluid meshes, we performed the grid and time-step size tests for the case when the normalized frequency $f/f_0 = 1$ with time-step corresponding to the coarse mesh is $\overline{\Delta t} = f\Delta t = 0.00694$, the medium grid is $\overline{\Delta t} = 0.00501$, and for the fine grid is $\overline{\Delta t} = 0.00357$. The flow is assumed as laminar and the simulation is carried out with a structural grid with 105 quadratic brick elements [24]. The response of the plate is characterized by the change of the relative displacement of the trailing edge with respect to that of the leading edge $A_{\mathrm{TE}}/A_{\mathrm{LE}}$ and the phase difference $\varphi$ between them. The comparison of $A_{TE}/A_{LE}$ under different resolutions is shown in Fig. 9. To reduce the computational cost and meanwhile, to obtain accurate results, we chose the medium-size mesh for the other simulations. The displacement of the trailing edge and the phase shift with varied forcing frequency is shown in Table 3.

It can be found from Table 3 that the present simulation results match well with the counterparts in the experiment. The peak displacement of the trailing edge is obtained when the forcing frequency equals the natural frequency $f_0$. At this point, the trailing edge displacement $A_{\mathrm{TE}}$ is 1.5 times larger than the $A_{\mathrm{LE}}$. This is the first resonance peak according to the analysis by Paraz et al. [44]. With the increase of forcing frequency, we find that the phase shift $\varphi$ experiences a continuous increase, indicating the strong interactions between fluid and structure with a large forcing frequency. The evolution of the *Z*-vorticity is depicted in Fig. 10. As seen, although the heave amplitude is relatively small compared with the length of the plate, the vortex street can still form and be observed clearly at the wake of the plate.

**Table 1 Comparison of drag coefficient and deformation in the absence of gravity and buoyancy when Re = 100**

| | $C_d$ | $D_x/b$ | $D_y/b$ |
|---|---|---|---|
| Tian et al. [42] | 1.02 | 2.34 | 0.67 |
| Mesh_fine | 1.05 | 2.31 | 0.675 |
| Mesh_medium | 1.06 | 2.31 | 0.678 |
| Mesh_coarse | 1.10 | 2.24 | 0.611 |

**Table 2 The drag coefficient and deformation in the absence of gravity and buoyancy when Re = 400**

| | $C_d$ | $D_x/b$ | $D_y/b$ |
|---|---|---|---|
| Tian et al. [42] | 0.94 | 2.34 | 0.68 |
| The present study | 0.99 | 2.28 | 0.647 |

**4.2 Resolution Verification.** A resolution study is performed to assess the appropriate mesh and time-step resolution by solving the laminar flow for $\mathrm{Re} = Uc/\nu = 2500$, $m^* = 0.02$, $\nu_s = 0.25$, $f^* = 1$, $\theta_m = 8$ deg, and $K_2 = 5$.

Three grids are generated: a coarse grid with 2,582,214 nodes and minimum spacing of $1.6 \times 10^{-3}c$ in each direction, a medium grid

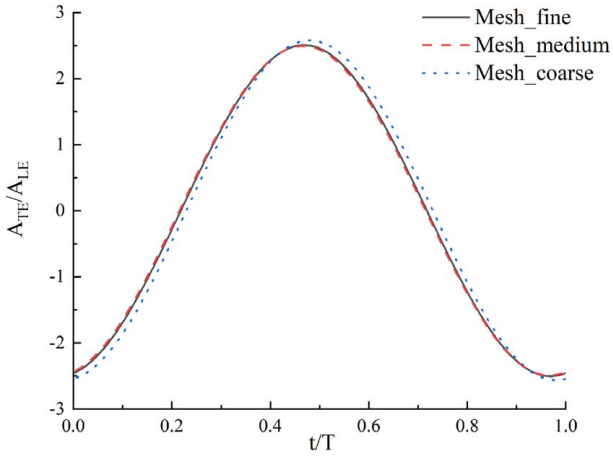


**Fig. 9 Results of the relative displacement of the trailing edge with three different meshes when $f/f_0 = 1$, $\mathrm{Re} = 6000$, $A_{\mathrm{LE}} = 0.004$ m, and rigidity $B = 0.018$ N·m**

**Table 3 The response of the trailing edge when the normalized frequency is varied for Re = 6000, $A_{\mathrm{LE}} = 0.004$ m, and rigidity $B = 0.018$ N·m**

| $f/f_0$ | $A_{\mathrm{TE}}/A_{\mathrm{LE}}$ in the experiment [44] | Present $A_{\mathrm{TE}}/A_{\mathrm{LE}}$ | $\varphi$ in the experiment (rad) [44] | Present $\varphi$(rad) |
|---|---|---|---|---|
| 0.53 | 1.53 | 1.60 | −0.065 | −0.060 |
| 0.73 | 2.10 | 2.29 | −0.17 | −0.19 |
| 1.00 | 2.58 | 2.49 | −0.40 | −0.43 |
| 2.10 | 1.60 | 1.62 | −0.82 | −0.81 |
| 2.50 | 1.49 | 1.55 | −0.86 | −0.88 |

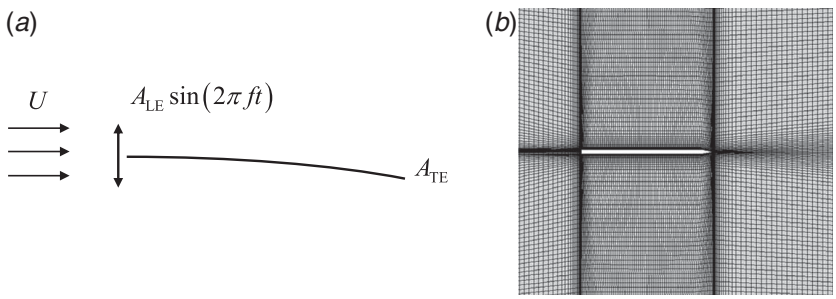


**Fig. 8 Sketch of the experimental setup of the flexible plate in a forced heave motion [44] (*a*) and the generated fine mesh around the plate (*b*)**

with 3,414,712 nodes and minimum spacing of $1.2\times10^{-3}c$ as shown in Fig. 11(*a*), and a fine grid with 5,592,570 nodes and minimum spacing of $8\times10^{-4}c$. All these three grids contain 103 blocks. The structural mesh contains 1532 quadratic brick elements. Furthermore, the non-dimensional time-step corresponding to the coarse grid is $\overline{\Delta t}=f\Delta t=0.00909$, the medium grid is $\overline{\Delta t}=0.00667$ and the time-step size for the fine one is $\overline{\Delta t}=0.00556$. The results of $C_T$ when three different grids and time-step sizes are used are shown in Fig. 11(*b*), and the mean coefficients $\overline{C_T}$, $\overline{C_P}$ as well as efficiency are compared in Table 4. Observed from the comparison, we can find that the medium resolution setup is sufficient to simulate the flow field around the caudal fin. Therefore, the medium grid with a time-step $\overline{\Delta t}=0.00667$ is used for the following simulations.

## 5 Results and Discussions

With the above code verifications, we applied the developed FSI tool to the rigid and flexible fins study as aforementioned. The flow considered is assumed as laminar and the Reynolds number under consideration is 2500, and under this Re number, the turbulence effect may play an insignificant role in the flow filed. The mass ratio is $m^*=0.02$, the rotation angle $\theta_m$ is 8 deg, the Poisson's ratio $\nu_s=0.25$, and the reduced frequency is $f^*=1$. These parameters are chosen to match those in the experiment by Ren et al. [33].

The predicted time-mean thrust, lateral forces, power input coefficients, and efficiency of the caudal fin, when flexural stiffness is varied, are summarized in Table 5. As seen from the table, the flexibility of the fin has a significant effect on the propulsion performance of the caudal fin. The $\bar{C}_T$, $\bar{C}_L$, $\bar{C}_P$, and $\eta$ vary remarkably when the caudal fin is assigned with different flexural rigidities. Compared with a rigid caudal fin, mostly, a flexible one is able to generate larger thrust, especially when $K_2=3$ the $\bar{C}_T$ increase by 197%, almost three times as large as that of a rigid one. In fact, when the rigidity reaches a sufficient big level, the thrust and efficiency show no difference with the rigid counterpart. Oppositely, when the fin is too flexible, i.e., $K_2=0.5$, despite the pronounced improvement of the efficiency, the thrust is very limited, which is even smaller than that of a rigid fin. These findings are consistent with the results in Refs. [23,45–48].

In terms of the power consumption, for flexible fins, it seems that the more thrust is generated, the more power input is needed. The

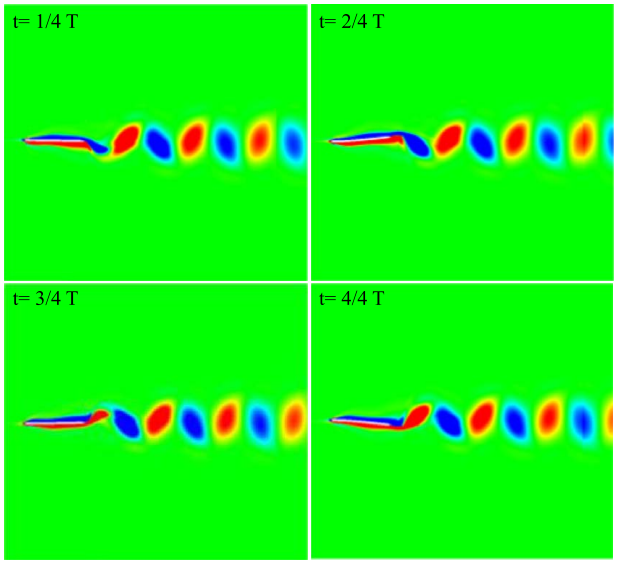


**Fig. 10 The vorticity contours in the *z*-direction during one heave period**

**Table 4 CFD mesh and time-step resolution study results**

| | $\overline{C_T}$ | $\overline{C_P}$ | $\eta$ | Number of processors used (2.1 GHz, Intel Xeon E5-2695) | Computational time per locomotion period |
|---|---|---|---|---|---|
| Mesh_Coarse | 1.545 | 8.945 | 0.173 | 72 | 17,994 s |
| Mesh_Medium | 1.599 | 9.131 | 0.175 | 103 | 28,355 s |
| Mesh_Fine | 1.616 | 9.227 | 0.175 | 103 | 52,240 s |

**Table 5 Summary of the time-mean thrust, lateral forces, power input coefficients, and efficiency**

| | $\bar{C}_T$ | $\bar{C}_L$ | $\bar{C}_P$ | $\eta$ |
|---|---|---|---|---|
| Rigid | 0.5995 | −0.0003 | 6.7056 | 0.0894 |
| $K_2=0.5$ | 0.4321 | 0.3317 | 1.8952 | 0.2280 |
| $K_2=3$ | 1.7784 | 0.9102 | 8.3562 | 0.2128 |
| $K_2=5$ | 1.5992 | 0.7002 | 9.1314 | 0.1751 |
| $K_2=50$ | 0.6944 | 0.00007 | 7.1918 | 0.0966 |

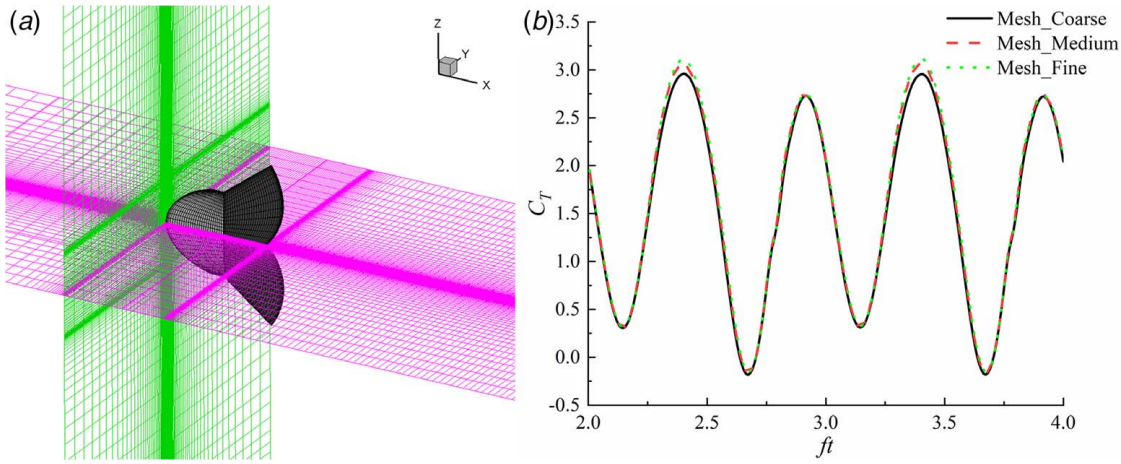


**Fig. 11 The generated medium fluid mesh around the caudal peduncle-fin model (*a*) and comparison of $C_T$ with different resolutions (*b*)**

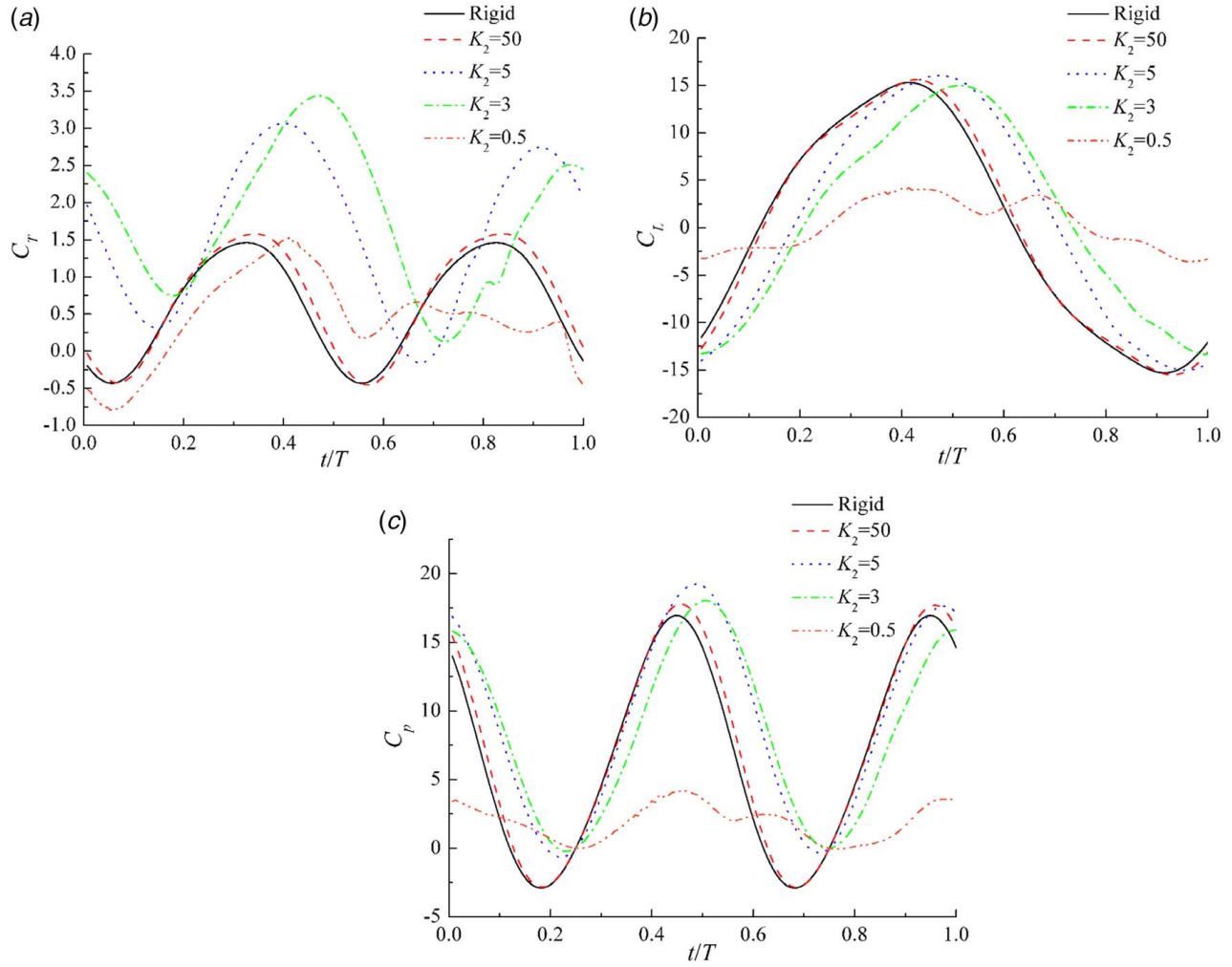


**Fig. 12 Instantaneous thrust coefficient $C_T$, lateral forces coefficient $C_L$, and power input coefficient $C_P$ over one flapping period when $K_2$ is 0.5 (dash dot line), 3 (dash dot line), 5 (dot line), 50 (dash line), and the fin is rigid (solid line)**

only exceptional case is $K_2 = 3$, in which the largest thrust is produced, while its needed power expenditure is not the most. In general, for compliant fins, the increase of power input is not as remarkable as the improvement of thrust, so the overall efficiency is enhanced compared with a rigid fin.

The time history of the thrust coefficient, the normalized lateral forces, and power input coefficient are demonstrated in Fig. 12. To facilitate description, these cases are categorized into three types: the least flexible cases (rigid find and the fin with $K_2 = 50$), the medium flexible cases (the fin with $K_2 = 3$ and $K_2 = 5$), and a

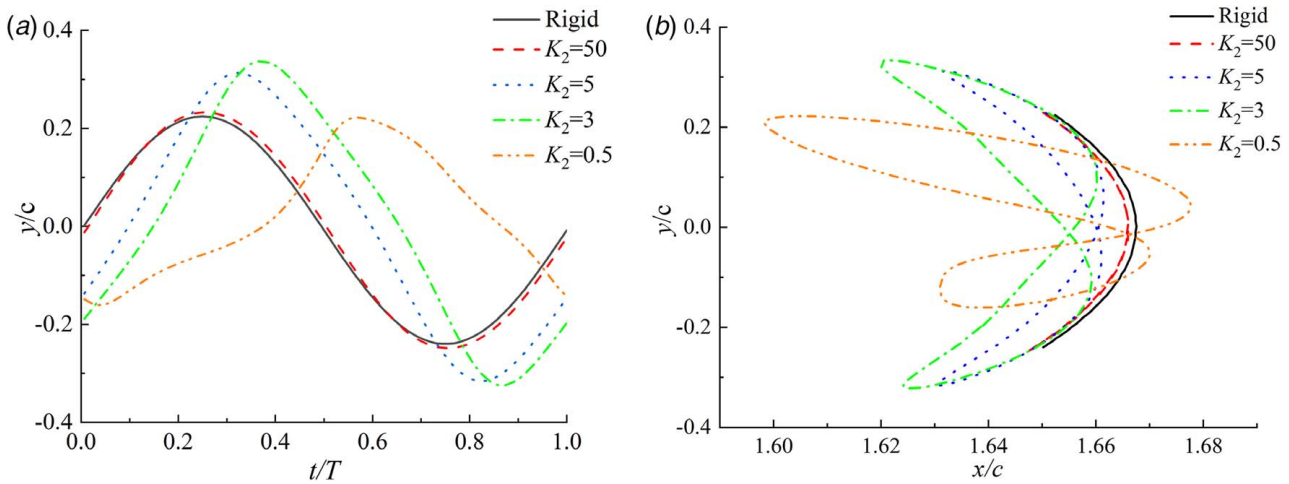


**Fig. 13 The time history of the *y*-direction displacement (*a*) and trajectory in *xy* plane (*b*) of the point *A* over one flapping period when $K_2$ is 0.5 (dash dot line), 3 (dash dot line), 5 (dot line), 50 (dash line), and the fin is rigid (solid line)**

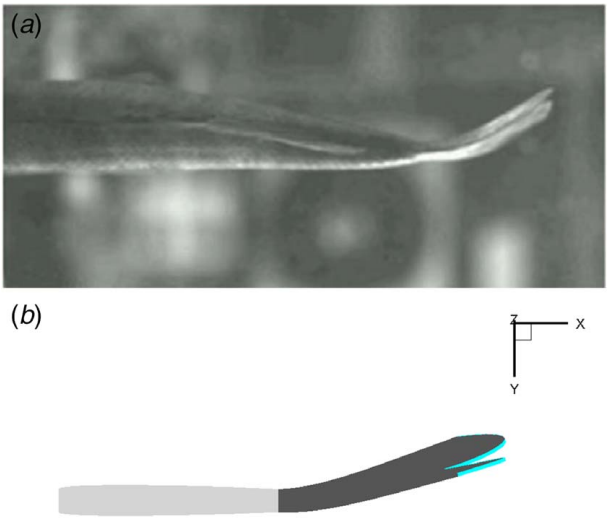


**Fig. 14 Images from a high-speed video of a live Bluegill fish in the flat motion adopted from Ref. [16] (*a*) and that of the current caudal peduncle-fin model (*b*) when $K_2 = 3$ at time $t+T$**

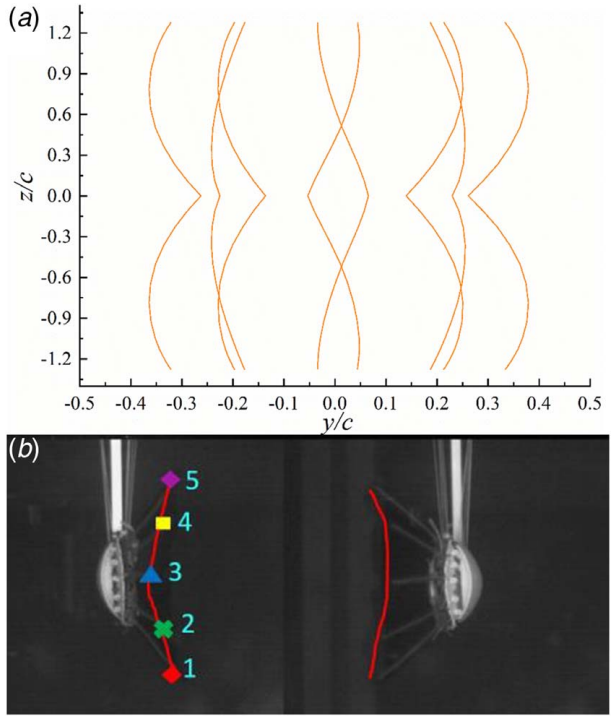


**Fig. 15 The fin deformation patterns of the trailing edge of the fin with $K_2 = 3$ (*a*) and posterior view of the robotic caudal fin in Ref. [50] (*b*)**

highly flexible case (the fin with $K_2 = 0.5$), according to their propulsion capability shown in Table 5.

As observed in Fig. 12(*a*), within one oscillation period, apart from the highly flexible case, the other two patterns both present two thrust peaks, though with different amplitudes. It is noted that the two crests of the rigid fin and the fin with $K_2 = 50$ are almost the same, indicating a symmetric feature between the fore and later half flapping. However, when the fin is more compliant, this symmetry is broken, and the emergence of the peaks is delayed significantly. In general, the thrust curves of the least flexible cases and those of the medium flexible cases present similar variation patterns. The $C_T$ curves of the medium flexible fins have two steep amplitude glens around peaks, which benefits faster acceleration maneuverability for the fish. In comparison, the $C_T$ curves of the least and highly flexible cases have lower peaks and flatter troughs, especially that of the fin with the smallest rigidity only fluctuate in a small range of amplitude in the second half flapping.

Nevertheless, all the power input coefficient curves almost have a similar fashion except for that of the highly flexible fin. The $C_P$ curve of the most compliant fin has a much smaller amplitude throughout most of the flapping cycle, so despite the least mean thrust output, it attains the most efficient propulsion. Interestingly, by comparing Fig. 12(*a*) with Fig. 12(*c*), it can be observed that the instantaneous thrust generation and power input almost reach the peaks at the same time, i.e., around the middle of the flapping period, when $K_2 = 3$.

As the power input plot, the lateral forces of the highly flexible fin presents a totally different fashion as others, of which all have clear peaks emerging around 2/5–3/5 T. However, owing to a continuous low lateral forces generated by the highly flexible fin, it may benefit to a straight-line cruising swimming for a fish.

The time history of the *y*-direction displacement and the trajectory of the point *A* at the upper trailing edge of the caudal fin shown in Fig. 2(*a*) within one flapping cycle is plotted in Fig. 13. It can be observed from Fig. 13(*a*) that the flexibility causes the delay of the appearance of the peak displacement. Meanwhile, like the instantaneous thrust curves, the motion of point *A* exhibits

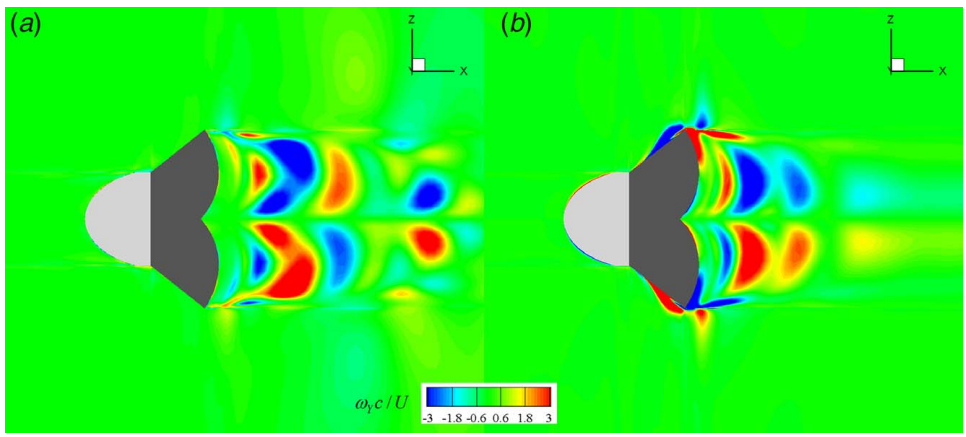


**Fig. 16 The wake flows contoured in *Y* vorticity of the flexible fin with $K_2 = 3$ (*a*) and the rigid fin in the *xz* plane of $y = 0.005$ m at the time $t + T$ (*b*)**

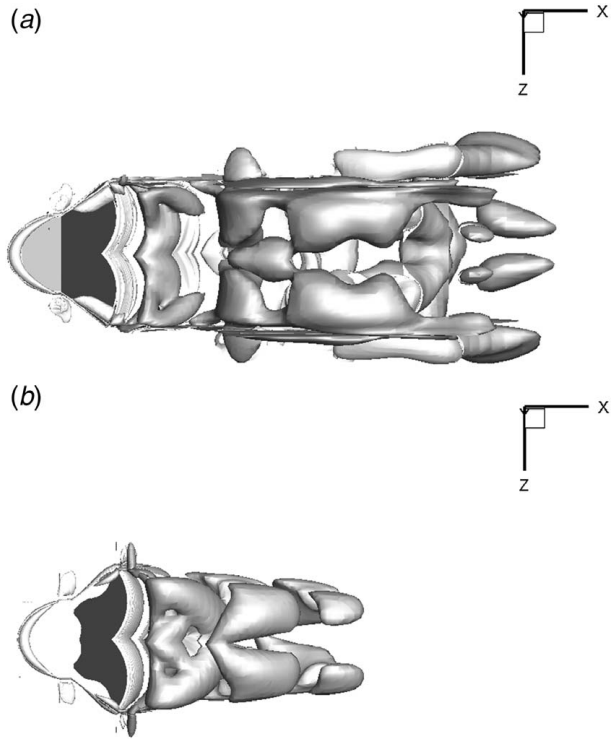


**Fig. 17 Iso-surface of vorticity field (*Q* criterion) in the wake of the flexible caudal fin ($K_2 = 3$) (*a*) and the rigid fin (*b*)**

three completely distinct fashions. When the fin is least flexible, the trajectories of the *A* are almost symmetric between the prior half and posterior half flapping, thus their motion curves are parabolas. However, when the fin is more compliant, their trajectories become figure-eight shapes, which is reminiscent of the typical orbital trajectories of the vortex-induced vibration of a cylinder [49].

The images obtained from a high-speed camera from the experiment of Esposito et al. [16] and that of the present caudal fin model are compared in Fig. 14. Owing to the reinforcement of the rigidity of the middle part of the caudal fin, it seems that the middle trailing edge has a phase delay compared with the

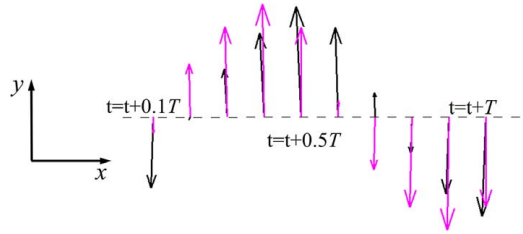


**Fig. 19 Force vectors of the flexible ($K_2 = 3$) (black) and rigid (pink) fin within one motion period**

dorsal and ventral parts in the present model, which is observed in the bending of the real fish caudal fin. This distinguishes the current simulation from most of the existing numerical studies in which only a uniformly distributed stiffness is considered. It can be further observed clearly in Fig. 15, in which the curvature patterns of the trailing edge of the caudal fin in *yz* plane during one flapping period is depicted, to demonstrate a highly three-dimensional deformation. Moreover, even though no active control of fin rays is imposed, a similar bending form to that of the robotic fin in the experiment [50] is observed. As a matter of fact, according to the results of the simulations by Zhu and Bi [14], more complex deformation patterns of caudal fins, e.g., W-shape, can be achieved by imposing specific distribution of the flexibility of fish rays (fin).

The wake flow of the rigid and flexible fins ($K_2 = 3$) are presented in Fig. 16. Two tip vortices shed from the dorsal- and ventral-most of the trailing edge of the caudal fin are formed parallel and alternatively. They have opposite rotation directions with one in counterclockwise while the other clockwise, and their vortices are approximately equal. These results match with those obtained in the experiments [16,33] using digital particle image velocimetry techniques, and to our knowledge, no similar vorticity patterns are reported by previous FSI studies. In comparison, the intensity of the vortices behind the flexible fin outperforms that of a rigid counterpart and it also has farther influence zone in the wake. As a result, the flexible fin generates larger thrust than the rigid one. This may explain the thrust augment shown in Fig. 12(*a*).

The wake structures of the flexible fin with $K_2 = 3$ and the rigid fin are depicted in Fig. 17. It can be observed that different wake patterns are presented between the two cases. Two trains of

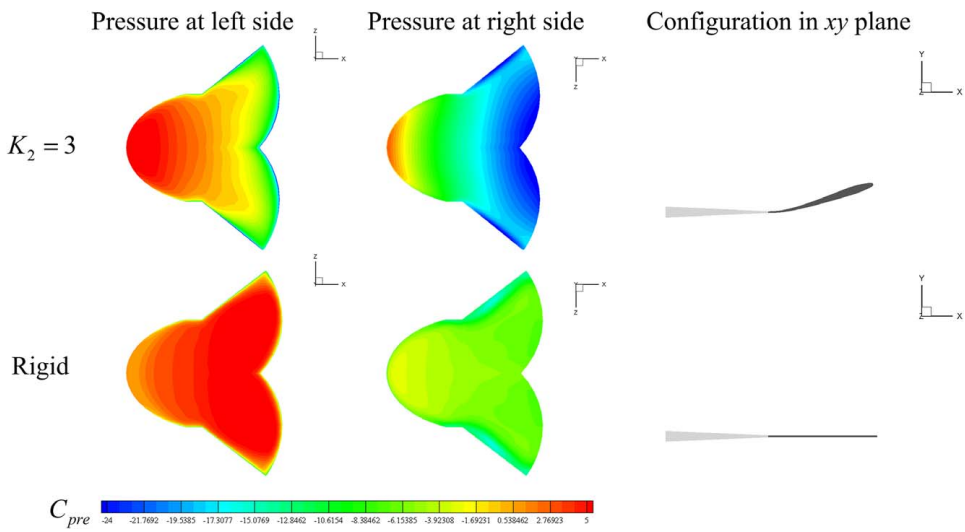


**Fig. 18 The pressure contours at the two sides of the flexible ($K_2 = 3$) and rigid model and their configurations in the *xy* plane at $t + 1/2\ T$. The left and right are defined from the viewpoint at posterior and $C_{pre} = (p - p_\infty)/0.5\rho_f U^2$.**

vortex rings are formed in their wake with distinct shapes. In comparison, the geometry of the wake of the deformable fin is more complex with some small vortices attached around the main vortex rings, while the wake of the rigid one is more regular. In addition, the wake structure of the rigid fin appears to be compressed in the spanwise direction compared with that of the flexible counterpart, which appears to expand in both dorsal and ventral directions and also along the further wake instead. This is consistent with the $Y$ vorticity contour in Fig. 16 indicating that a three-dimensional deformation of the fin makes the wake pattern more complex.

The pressure distribution of the caudal peduncle-fin model is plotted in Fig. 18. It can be observed that the left side of the rigid fin is covered by high pressure which becomes stronger along the trailing edge, while low pressure mainly occupies the surface of a flexible fin near the tip. As for the right side, a remarkable low-pressure zone is observed at the flexible fin surface, and in comparison, the rigid fin surface has a smaller pressure gradient. It seems hard to evaluate the thrust generation only by the similar pressure difference at the two sides between the flexible and rigid fin. However, with a close inspection of the configurations of the two models in the $xy$ plane, one may find that the flexible fin is better oriented in the negative $x$-direction, which can be further found in Fig. 19. The forces generated by a rigid fin may have a larger magnitude than those of a flexible one, but the forces of the latter are better pointed in the thrust direction, which contributes to the thrust enhancement for a flexible fin.

## 6 Conclusions

In this work, a fully coupled FSI solver is proposed by combining our in-house fluid solver with a finite element method based code CalculiX via preCICE. Three FSI validations are conducted to verify this multi-physics solver. Beyond that, the developed tool is applied to study the propulsive performance of a caudal peduncle-fin swimmer with a non-uniform distribution of stiffness. It is found that the compliance of the caudal fin has a significant impact on its propulsion performance. With the parameters selected in this paper, the flexible fins outperform the rigid counterparts in terms of thrust generation and/or propulsion efficiency. The degree to which is profoundly affected by the assigned inflexibility. Interestingly, via apposing inhomogeneous distribution of the rigidity of fins, some curvature patterns of the caudal fin, observed from live fish and bio-inspired experimental robotic fish, are presented from our simulation results.

It must be noted that due to the simplified model for the distribution of caudal fin rigidity, the effect of the more complex situation, such as the variations of the flexibility in spanwise direction of the fin, is not investigated. In addition, the chordwise distribution of flexural rigidity of a real fish fin is non-uniform while we assumed it is uniform in this study. Obviously, more in-depth investigations are needed to elucidate the abovementioned effects for a better understanding of this problem.

## Acknowledgment

This work used the Cirrus UK National Tier-2 HPC Service at EPCC[2] funded by the University of Edinburgh and EPSRC (EP/P020267/1) and ARCHIE-WeSt High Performance Computer[3] based at the University of Strathclyde. The first author would like to acknowledge Dr. Benjamin Uekermann in the Technical University of Munich for his kind suggestions about the coding works of the FSI coupling and also thank China Scholarship Council (CSC) for the financial support during his study in the UK.

[2]http://www.cirrus.ac.uk
[3]https://www.archie-west.ac.uk

## References

[1] Bandyopadhyay, P. R., 2005, "Trends in Biorobotic Autonomous Undersea Vehicles," IEEE J. Oceanic Eng., **30**(1), pp. 109–139.
[2] Luo, Y., Pan, G., Huang, Q., Shi, Y., and Lai, H., 2019, "Parametric Geometric Model and Shape Optimization of Airfoils of a Biomimetic Manta Ray Underwater Vehicle," J. Shanghai Jiaotong University (Science), **24**(3), pp. 402–408.
[3] Salazar, R., Fuentes, V., and Abdelkefi, A., 2018, "Classification of Biological and Bioinspired Aquatic Systems: A Review," Ocean Eng., **148**, pp. 75–114.
[4] Triantafyllou, G. S., Triantafyllou, M., and Grosenbaugh, M., 1993, "Optimal Thrust Development in Oscillating Foils With Application to Fish Propulsion," J. Fluids Struct., **7**(2), pp. 205–224.
[5] Dong, H., Mittal, R., and Najjar, F., 2006, "Wake Topology and Hydrodynamic Performance of Low-Aspect-Ratio Flapping Foils," J. Fluid Mech., **566**, pp. 309–343.
[6] Wolfgang, M. J., Anderson, J. M., Grosenbaugh, M. A., Yue, D. K., and Triantafyllou, M. S., 1999, "Near-Body Flow Dynamics in Swimming Fish," J. Exp. Biol., **202**(17), pp. 2303–2327.
[7] Kern, S., and Koumoutsakos, P., 2006, "Simulations of Optimized Anguilliform Swimming," J. Exp. Biol., **209**(24), pp. 4841–4857.
[8] Bozkurttas, M., Mittal, R., Dong, H., Lauder, G. V., and Madden, P., 2009, "Low-Dimensional Models and Performance Scaling of a Highly Deformable Fish Pectoral Fin," J. Fluid Mech., **631**, pp. 311–342.
[9] Heathcote, S., and Gursul, I., 2007, "Flexible Flapping Airfoil Propulsion at Low Reynolds Numbers," AIAA J., **45**(5), pp. 1066–1079.
[10] Longzhen, D., Guowei, H., and Xing, Z., 2016, "Self-Propelled Swimming of a Flexible Plunging Foil Near a Solid Wall," Bioinspiration Biomimetics, **11**(4), p. 046005.
[11] Lauder, G. V., 1982, "Structure and Function in the Tail of the Pumpkinseed Sunfish (*Lepomis gibbosus*)," J. Zool., **197**(4), pp. 483–495.
[12] Park, Y.-J., Huh, T. M., Park, D., and Cho, K.-J., 2014, "Design of a Variable-Stiffness Flapping Mechanism for Maximizing the Thrust of a Bio-Inspired Underwater Robot," Bioinspiration Biomimetics, **9**(3), p. 036002.
[13] Kancharala, A. K., and Philen, M. K., 2016, "Optimal Chordwise Stiffness Profiles of Self-Propelled Flapping Fins," Bioinspiration Biomimetics, **11**(5), p. 056016.
[14] Zhu, Q., and Bi, X., 2017, "Effects of Stiffness Distribution and Spanwise Deformation on the Dynamics of a Ray-Supported Caudal Fin," Bioinspiration Biomimetics, **12**(2), p. 026011.
[15] Jayne, B. C., and Lauder, G. V., 1995, "Speed Effects on Midline Kinematics During Steady Undulatory Swimming of Largemouth Bass, Micropterus Salmoides," J. Exp. Biol., **198**(2), pp. 585–602.
[16] Esposito, C. J., Tangorra, J. L., Flammang, B. E., and Lauder, G. V., 2012, "A Robotic Fish Caudal Fin: Effects of Stiffness and Motor Program on Locomotor Performance," J. Exp. Biol., **215**(1), pp. 56–67.
[17] Ren, Z., Yang, X., Wang, T., and Wen, L., 2016, "Hydrodynamics of a Robotic Fish Tail: Effects of the Caudal Peduncle, Fin Ray Motions and the Flow Speed," Bioinspiration Biomimetics, **11**(1), p. 016008.
[18] Jameson, A., Schmidt, W., and Turkel, E. L. I., 1981, "Numerical Solution of the Euler Equations by Finite Volume Methods Using Runge Kutta Time Stepping Schemes," 14th Fluid and Plasma Dynamics Conference, June 23–25, American Institute of Aeronautics and Astronautics.
[19] Alonso, J., and Jameson, A., 1994, "Fully-Implicit Time-Marching Aeroelastic Solutions," 32nd Aerospace Sciences Meeting and Exhibit, Reno, NV, Jan. 10–13, p. 56.
[20] Xiao, Q., and Liao, W., 2010, "Numerical Investigation of Angle of Attack Profile on Propulsion Performance of an Oscillating Foil," Comput. Fluids, **39**(8), pp. 1366–1380.
[21] Xiao, Q., Liao, W., Yang, S., and Peng, Y., 2012, "How Motion Trajectory Affects Energy Extraction Performance of a Biomimic Energy Generator With an Oscillating Foil?," Renewable Energy, **37**(1), pp. 61–75.
[22] Liu, W., Xiao, Q., and Cheng, F., 2013, "A Bio-Inspired Study on Tidal Energy Extraction With Flexible Flapping Wings," Bioinspiration Biomimetics, **8**(3), p. 036011.
[23] Shi, G., Qing, X., Qiang, Z., and Wei, L., 2019, "Fluid-Structure Interaction Modeling on a 3D Ray-Strengthened Caudal Fin," Bioinspiration Biomimetics, **14**(3), p. 036012.
[24] Dhondt, G., 2004, *The Finite Element Method for Three-Dimensional Thermomechanical Applications*, John Wiley & Sons, New York.
[25] Liu, W., Xiao, Q., and Zhu, Q., 2016, "Passive Flexibility Effect on Oscillating Foil Energy Harvester," AIAA J., **54**(4), pp. 1172–1187.
[26] Bungartz, H.-J., Lindner, F., Gatzhammer, B., Mehl, M., Scheufele, K., Shukaev, A., and Uekermann, B., 2016, "preCICE—A Fully Parallel Library for Multi-Physics Surface Coupling," Comput. Fluids, **141**, pp. 250–258.
[27] Degroote, J., Bathe, K.-J., and Vierendeels, J., 2009, "Performance of a New Partitioned Procedure Versus a Monolithic Procedure in Fluid–Structure Interaction," Comput. Struct., **87**(11–12), pp. 793–801.
[28] Haelterman, R., Bogaers, A. E. J., Scheufele, K., Uekermann, B., and Mehl, M., 2016, "Improving the Performance of the Partitioned QN-ILS Procedure for Fluid–Structure Interaction Problems: Filtering," Comput. Struct., **171**, pp. 9–17.
[29] Tsai, H. M., Wong, A. S. F., Cai, J., Zhu, Y., and Liu, F., 2001, "Unsteady Flow Calculations With a Parallel Multiblock Moving Mesh Algorithm," AIAA J., **39**(6), pp. 1021–1029.
[30] Lindner, F., Mehl, M., and Uekermann, B., 2017, "Radial Basis Function Interpolation for Black-Box Multi-Physics Simulations," VII International Conference on Computational Methods for Coupled Problems in Science and Engineering, Rhodes, Greece, June 12–14, pp. 1–12.

[31] Luo, Y., Xiao, Q., Shi, G., Wen, L., Chen, D., and Pan, G., 2020, "A Fluid–Structure Interaction Solver for the Study on a Passively Deformed Fish Fin With Non-Uniformly Distributed Stiffness," J. Fluids Struct., **92**, p. 102778.
[32] Flammang, B. E., and Lauder, G. V., 2008, "Speed-Dependent Intrinsic Caudal Fin Muscle Recruitment During Steady Swimming in Bluegill Sunfish, *Lepomis Macrochirus*," J. Exp. Biol., **211**(4), pp. 587–598.
[33] Ren, Z., Hu, K., Wang, T., and Wen, L., 2016, "Investigation of Fish Caudal Fin Locomotion Using a Bio-Inspired Robotic Model," Int. J. Adv. Rob. Syst., **13**(3), p. 87.
[34] Liu, G., Geng, B., Zheng, X., Xue, Q., Wang, J., and Dong, H., 2018, "An Integrated High-Fidelity Approach for Modeling Flow-Structure Interaction in Biological Propulsion and Its Strong Validation," 2018 AIAA Aerospace Sciences Meeting, Jan. 8–12, American Institute of Aeronautics and Astronautics.
[35] Olivier, M., Morissette, J.-F., and Dumas, G., 2009, "A Fluid-Structure Interaction Solver for Nano-Air-Vehicle Flapping Wings," 19th AIAA Computational Fluid Dynamics, June 22–25, American Institute of Aeronautics and Astronautics.
[36] Wood, C., Gil, A. J., Hassan, O., and Bonet, J., 2010, "Partitioned Block-Gauss–Seidel Coupling for Dynamic Fluid–Structure Interaction," Comput. Struct., **88**(23–24), pp. 1367–1382.
[37] Nakata, T., and Liu, H., 2012, "A Fluid–Structure Interaction Model of Insect Flight With Flexible Wings," J. Comput. Phys., **231**(4), pp. 1822–1847.
[38] Habchi, C., Russeil, S., Bougeard, D., Harion, J.-L., Lemenand, T., Ghanem, A., Valle, D. D., and Peerhossaini, H., 2013, "Partitioned Solver for Strongly Coupled Fluid–Structure Interaction," Comput. Fluids, **71**, pp. 306–319.
[39] Dettmer, W., and Perić, D., 2006, "A Computational Framework for Fluid–Structure Interaction: Finite Element Formulation and Applications," Comput. Methods Appl. Mech. Eng., **195**(41–43), pp. 5754–5779.
[40] Matthies, H. G., and Steindorf, J., 2003, "Partitioned Strong Coupling Algorithms for Fluid–Structure Interaction," Comput. Struct., **81**(8–11), pp. 805–812.
[41] Luhar, M., and Nepf, H. M., 2011, "Flow-Induced Reconfiguration of Buoyant and Flexible Aquatic Vegetation," Limnol. Oceanogr., **56**(6), pp. 2003–2017.
[42] Tian, F.-B., Dai, H., Luo, H., Doyle, J. F., and Rousseau, B., 2014, "Fluid–Structure Interaction Involving Large Deformations: 3D Simulations and Applications to Biological Systems," J. Comput. Phys., **258**, pp. 451–469.
[43] Paraz, F., Schouveiler, L., and Eloy, C., 2016, "Thrust Generation by a Heaving Flexible Foil: Resonance, Nonlinearities, and Optimality," Phys. Fluids, **28**(1), p. 011903.
[44] Paraz, F., Eloy, C., and Schouveiler, L., 2014, "Experimental Study of the Response of a Flexible Plate to a Harmonic Forcing in a Flow," Comptes Rendus Mécanique, **342**(9), pp. 532–538.
[45] Dai, H., Luo, H., Sousa, P. J. S. A. F. D., and Doyle, J. F., 2012, "Thrust Performance of a Flexible Low-Aspect-Ratio Pitching Plate," Phys. Fluids, **24**(10), p. 101903.
[46] Olivier, M., and Dumas, G., 2016, "A Parametric Investigation of the Propulsion of 2D Chordwise-Flexible Flapping Wings at Low Reynolds Number Using Numerical Simulations," J. Fluids Struct., **63**, pp. 210–237.
[47] Zhang, Y., Zhou, C., and Luo, H., 2017, "Effect of Mass Ratio on Thrust Production of an Elastic Panel Pitching or Heaving Near Resonance," J. Fluids Struct., **74**, pp. 385–400.
[48] Shi, G., Xiao, Q., and Zhu, Q., 2017, "A Study of 3D Flexible Caudal Fin for Fish Propulsion," ASME 2017 36th International Conference on Ocean, Offshore and Arctic Engineering, American Society of Mechanical Engineers, p. V07AT06A052.
[49] Wang, E., Xiao, Q., and Incecik, A., 2017, "Three-Dimensional Numerical Simulation of Two-Degree-of-Freedom VIV of a Circular Cylinder With Varying Natural Frequency Ratios at Re=500," J. Fluids Struct., **73**, pp. 162–182.
[50] Hu, K., Ren, Z., Wang, Y., Wang, T., and Wen, L., 2016, "Quantitative Hydrodynamic Investigation of Fish Caudal Fin Cupping Motion Using a Bio-Robotic Model," 2016 IEEE International Conference on Robotics and Biomimetics (ROBIO), Qingdao, China, Dec. 3–7, pp. 295–300.